PHYSICAL REVIEW D **87,** 084008 (2013)

Impact of higher-order modes on the detection of binary black hole coalescences

Larne Pekowsky, James Healy, Deirdre Shoemaker, and Pablo Laguna

Center for Relativistic Astrophysics and School of Physics, Georgia Institute of Technology, Atlanta, Georgia 30332, USA

(Received 9 October 2012; published 2 April 2013)

The inspiral and merger of black hole binary systems are a promising source of gravitational waves for the array of advanced interferometric ground-based gravitational-wave detectors currently being commissioned. The most effective method to look for a signal with a well understood waveform, such as the binary black hole signal, is matched filtering against a library of model waveforms. While current model waveforms are comprised solely of the dominant radiation mode, the quadrupole mode, it is known that there can be significant power in the higher-order modes for a broad range of physically relevant source parameters during the merger of the black holes. The binary black hole waveforms produced by numerical relativity are accurate through late inspiral, merger, and ringdown and include the higher-order modes. The available numerical-relativity waveforms span an increasing portion of the physical parameter space of unequal mass, spin and precession. In this paper, we investigate the degree to which gravitational-wave searches could be improved by the inclusion of higher modes in the model waveforms, for signals with a variety of initial mass ratios and generic spins. Our investigation studies how well the quadrupole-only waveform model matches the signal as a function of the inclination and orientation of the source and how the modes contribute to the distance reach into the Universe of Advanced LIGO for a fixed set of internal source parameters. The mismatch between signals and quadrupole-only waveforms can be large, dropping below 0.97 for up to 65% of the source sky for the nonprecessing cases we studied, and over a larger area in one precessing case. There is a corresponding 30% increase in detection volume that could be achieved by adding higher modes to the search; however, this is mitigated by the fact that the mismatch is largest for signals which radiate the least energy and to which the search is therefore least sensitive. Likewise, the mismatch is largest in the directions from the source along which the least energy is radiated.

DOI: 10.1103/PhysRevD.87.084008 PACS numbers: 04.25.D−, 04.25.dg, 04.30.Db, 04.80.Nn

I. INTRODUCTION

The merger of a binary black hole (BBH) system has long been considered a strong source of gravitational waves for ground- and space-based gravitational-wave observatories. These mergers are characterized by 15 parameters: nine intrinsic to the black hole systems (two black hole masses, two spin vectors and eccentricity) and six extrinsic to the source (binary orientation vector, sky position and distance). The LIGO and Virgo detectors have recently completed a joint run during which inspiral horizon distances exceeded 40 Mpc [1] and new upper limits have been placed on the rates of such events [2]. These observatories are currently being upgraded and when the new design sensitivities are achieved they will have ranges up to ten times greater and hence volumes 1000 times greater. By the end of this decade LIGO and Virgo, along with GEO, will be joined by KAGRA in Japan and possibly the proposed LIGO India, greatly increasing not only the range of the global network but also the ability to recover information about the sources [3].

When the theoretical model of the gravitational waveform is well understood, the most effective method to search and recover a gravitational-wave signal is matched filtering against a library of model waveforms called a *template bank* [4]. The ability of such a templated search to detect signals is dependent on four factors:

(i) The frequency-dependent sensitivity of the detector. Throughout this paper we use the targeted aLIGO *zero-detuned, high-power* [5] sensitivity curve.
(ii) The direction-dependent sensitivity of the detector. This is a fixed property of interferometric instruments and the orientation on Earth's surface. Any one detector will have blind spots; one motivation for constructing a network of detectors is to provide more complete coverage of the sky. We will not consider multidetector searches in this paper.
(iii) The total energy radiated by the source from the time it enters the sensitive band of the detectors. This provides an upper limit on the ability to detect different signals; a source that radiates less energy will be visible out to a smaller distance than one that radiates more energy, all other factors being equal.
(iv) The ability of the templates to extract signal power from the background noise.

In this paper we will be concerned with the last two points.

For the BBH systems potentially observable by ground-based detectors, astrophysical processes place few constraints on the intrinsic physical parameters that characterize the emission of radiation from these cataclysmic events, thus placing the burden on source models to cover nearly the full compliment of physical parameters. Rigorous requirements from matched filtering place an additional burden on the source models. In order for the model waveforms

to match potential signals to within a given tolerance, we need not only enough waveforms to cover the parameter space but also each waveform must represent nature effectually enough to ensure the signal does not fall through cracks in the template bank and faithfully enough to recover the source parameters.

One source of mismatch with nature is the truncation of the spherical harmonic series in which we have decomposed the model waveform. Current template waveforms are only of the dominant, quadrupole mode, although we know that generic signals will have many excited harmonics present when detected. Figure 1 shows the ratio of several nondominant modes to the dominant mode for two nonspinning systems; note that for the system where the masses of the component holes are not equal the next-to-leading mode is within an order of magnitude of the quadrupole mode, suggesting that accounting for additional modes may be important for detection, especially as the mass ratio strongly deviates from 1 and generic spins are explored.

This paper builds on previous work by ourselves and other authors. In Refs. [6,7], we conducted a preliminary study on higher modes for spinning, equal-mass systems comparing numerical relativity waveforms containing the largest five harmonics to an equal-mass nonspinning system of just the dominant mode. We found that for low spins, the nonspinning dominant mode was an effective model waveform. McWilliams *et al.* [8] found that over a range of the source orientations, the equal-mass waveform was effective at detecting moderate mass ratios over source orientations.

In this paper we utilize numerical-relativity waveforms to represent both the signals that will be received by detectors, and the templates that will be used to search for these signals. In practice the set of available NR signals is not dense enough to use for searches, so numerous other model waveforms are used. The waveforms currently used or currently being considered include various post-Newtonian approximations (see Appendix A of Ref. [9] and references therein), phenomenological models such as [10], and effective-one-body models calibrated against numerical relativity ("EOBNR") [11]. Of these, the last is the only family which provides higher-order modes in the current implementations. Brown *et al.* [12] is exploring the value added of higher modes in EOBNR models of unequal-mass waveforms.

In this paper we investigate the degree to which inclusion of additional terms of the spherical harmonic series to template waveforms could improve matched-filter-based searches. We use numerical relativity (NR) waveforms as both signal and template, and we consider both unequal masses and some generic spins generated by the MAYA code. We study how well the quadrupole-only model waveform matches the signal as a function of the inclination and orientation of the source and determine how the volume reach of advanced LIGO depends on the inclusion/exclusion of nondominant harmonics in the model waveforms. We concentrate on system masses greater than $100M_{\odot}$ to give the NR portion of the waveform prominence and negate the need for post-Newtonian information. Our findings show that for nonprecessing signals up to 65% of source orientations can be missed when using only the quadrupole mode, implying a 30% gain in detection volume which could be achieved by including higher modes. For our most precessing case when using the quadrupole mode only the loss of source orientations is nearly 100% and the potential gain in volume over which such systems could be detected is 45%. These potential gains in volume are mitigated by the fact that the mismatch is largest for signals which radiate the least energy and to which, therefore, the search is least sensitive. Likewise, the mismatch is largest in the directions from the source along which the least energy is radiated. Finally, we do a preliminary investigation into how the series truncation might impact parameter estimation by exploring a potential degeneracy between mass and inclination for full waveforms in the last section of this paper.

We proceed as follows: In Sec. II we introduce our methodology for matched filtering, and in Sec. III the NR waveforms used in all of our studies. In Sec. IV we consider various aspects of the overlaps between the dominant

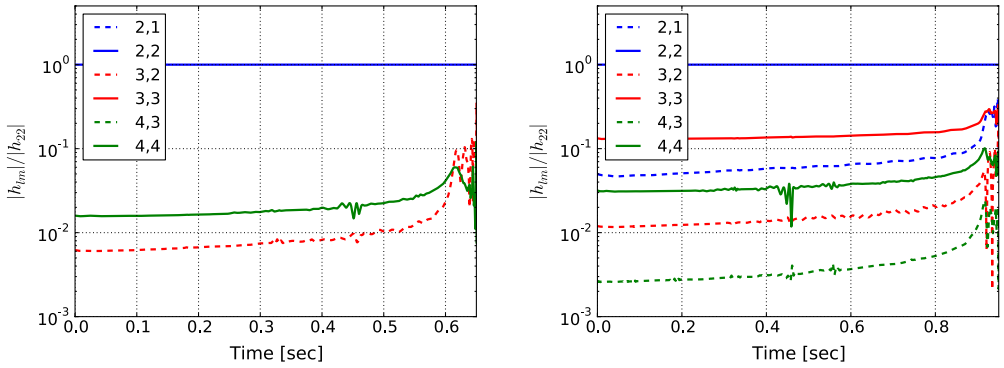

FIG. 1 (color online). Relative amplitude of higher modes for nonspinning $q = 1$ (left) and $q = 4$ (right) systems. For the $q = 1$ system the (4,4) and (3,2) modes are about 2 orders of magnitude smaller than the (2,2). All others are less than 10^{-3}. For the $q = 4$ the (3,3) mode is within a factor of 10 of the dominant (2,2) mode, and several other modes are within another factor of 10.

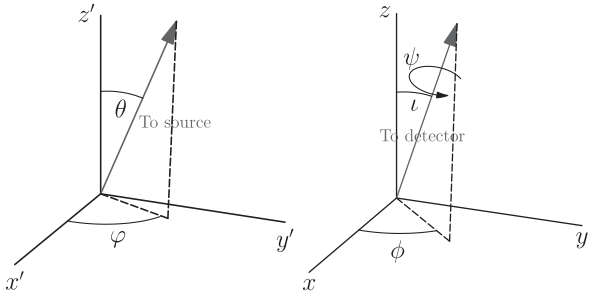

FIG. 2. Definition of angles used in this paper. Left: The angles used at the detector, looking at the source. Although ψ refers to a rotation of the plane containing the source, we associate it with the detector because it enters the analysis though the antenna pattern. Right: The angles used at the source, looking towards the detector. These are the angles in which the spherical harmonics are written.

mode and the higher modes. In Sec. V we examine the volume of the Universe that is accessible to advanced detectors using quadrupole-only waveforms and hypothetical ideal waveforms containing most of the modes, for several cases. We conclude in Sec. VI that the smallest overlaps are obtained for systems and source orientations which radiate the least total power, and hence have the smallest accessible volumes even when an ideal waveform is used. In this section we also present a first look at the implications of higher modes for parameter estimation.

Conventions: Throughout this paper we adopt the following conventions. We denote the Fourier transform of a function $g(t)$ with a tilde, as $\tilde{g}(f)$. We characterize the mass ratio of a BBH system by $q = m_1/m_2$ with $m_1 \geq m_2$. The relation of the source to the detector is specified by five angles. Two (ι, ϕ) place the detector in coordinates centered at the source; it is these angles in which the decomposition into spherical harmonics is performed. Two (θ, φ) place the source in the sky of the detector. The final angle, ψ, determines the relative rotation between these two coordinate systems; we associate ψ with the source because in what follows we will treat it similarly to ι and ϕ. We define these angles in Fig. 2. The final parameter connecting the source and detector is the distance between them; we will be concerned with the maximum distance at which the source can be detected and will determine this value in what follows.

II. MATCHED-FILTER SEARCHES FOR GRAVITATIONAL WAVES

The response of an interferometric detector is described by an *antenna pattern* [13],

$$F_+ = -\frac{1}{2}(1+\cos^2\theta)\cos 2\varphi\cos 2\psi - \cos\theta\sin 2\varphi\sin 2\psi,$$
$$F_\times = \frac{1}{2}(1+\cos^2\theta)\cos 2\varphi\sin 2\psi - \cos\theta\sin 2\varphi\cos 2\psi. \quad (1)$$

Following [14] we rewrite this in the more convenient form

$$F_+ = F_0\cos 2(\psi+\psi_0), \qquad F_\times = F_0\sin 2(\psi+\psi_0), \quad (2)$$

where

$$F_0 = \sqrt{((1+\cos^2\theta)/2)^2\cos^2 2\varphi + \cos^2\theta\sin^2 2\varphi}$$

and

$$\tan 2\psi_0 = \frac{\cos\theta}{(1+\cos^2\theta)/2}\tan 2\varphi.$$

For reference we show the antenna pattern in Fig. 3.

For gravitational waves, the intrinsic characteristics of a source are fully encapsulated in the polarization strains h_+ and $h_\times$. When an incoming gravitational wave is incident on the detector the strains give rise to a signal s given by

$$\begin{aligned} s(\theta,\varphi,\iota,\phi,\psi,t) &= F_+(\theta,\varphi,\psi)h_+(\iota,\phi,t) + F_\times(\theta,\varphi,\psi)h_\times(\iota,\phi,t) \\ &= F_0(\theta,\varphi)h(\psi,\iota,\phi,t), \end{aligned} \quad (3)$$

where we have used Eq. (2) and defined

$$h(\psi,\iota,\phi,t) = \cos 2(\psi+\psi_0)h_+(\iota,\phi,t) + \sin 2(\psi+\psi_0)h_\times(\iota,\phi,t).$$

The output of the detector is then $s+n$, where n is the noise of the detector. Following standard practice we incorporate the noise only as $S_n(f)$ and do not add it to the signal in what follows. We will take h in Eq. (3) to be the output of a numerical simulation, to be discussed in the following section.

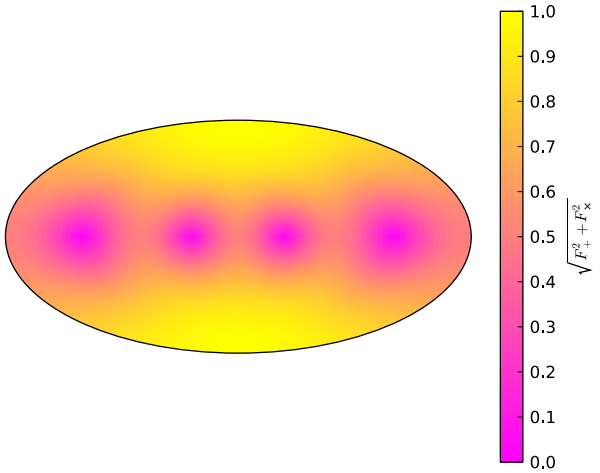

FIG. 3 (color online). Antenna pattern for an interferometric gravitational-wave detector in source-centric coordinates, φ horizontally and θ vertically. The arms lie along $\theta = \pi/2$, $\varphi = 0, \pi/2$ respectively. Such a detector is most sensitive to signals directly overhead or below, and least sensitive to signals in the plane of the arms. The sensitivity drops to zero along the lines between the arms, $\theta = \pi/2$, $\varphi = \pm\pi/4$ and $\theta = \pi/2$, $\varphi = \pm 3\pi/4$.

We now briefly review some of the data analysis framework employed in current LIGO/Virgo searches, and which will be used throughout this paper. An inner product on the space of real, time-dependent waveforms $A(t)$ and $B(t)$, with respect to a given noise curve described by a power spectral density $S_n(f)$, is

$$A(t)|B(t) = 4\mathrm{Re}\int_0^\infty df \frac{\tilde{A}(f)\tilde{B}^\star(f)}{S_n(f)}. \quad (4)$$

In stationary, Gaussian noise, the optimal measure of the presence of a gravitational wave signal that matches a model waveform, called a *template*, is the signal-to-noise-ratio (SNR) denoted by ρ, with

$$\rho^2 = \frac{(s|h_+)^2}{(h_+|h_+)}, \quad (5)$$

and where we are studying the response of a single detector to one polarization, typically taken to be h_+. We note in passing that in a multidetector search the data streams from all instruments will be filtered against the same h_+, and that the source angles ι, ϕ will be the same at all detectors. However, the orientations of the different detectors will provide different values of ψ, making the detectors sensitive to different combinations of the polarization. In addition each detector's F_0 will have a different dependence on θ, φ, providing coverage of regions of the sky to which any one detector might be insensitive.

The signal will arrive at an unknown time which we identify as the time of coalescence and denote t_0. We assume the template waveform h is a good approximation to the signal s, and search for the signal at all times by shifting the template. This has the effect in the Fourier domain of changing $\tilde{h}(f)$ to $\tilde{h}(f)\exp(-2\pi i f t_0)$. The signal will also have an unknown phase at the time of coalescence, corresponding to the value of ϕ in Fig. 2, which we denote ϕ_0. This introduces an additional factor of $\exp(2\pi i\phi_0)$. In practice, this leads the SNR to be evaluated as

TABLE I. Simulations used. The 28 simulations' initial parameters and grid structures are listed. The table is split into three groups: nonspinning, equal mass with spin, and precessing spins. The table contains $q = m_+/m_-$, the bare puncture masses m_{b+}/M and m_{b-}/M; the nondimensional spins, $\chi_i = S_i/m_i^2$; the initial momentum, p_+/M; the initial separation, d/M; the outer boundary, R_b/M; and the resolution on the finest refinement level M/h_{fine}. If only one spin value is listed, the spin is aligned with the initial angular momentum.

ID	q	m_{b+}/M	m_{b-}/M	χ_+	χ_-	p_+/M	d/M	R_b/M	M/h_{fine}
Q01	1.00	0.485923	0.485923	0.0	0.0	(−0.00098038, 0.096107, 0)	10.00	317.44	103
Q02	1.15	0.520973	0.451009	0.0	0.0	(−0.00097306, 0.095648, 0)	10.00	317.44	103
Q03	1.30	0.551561	0.420763	0.0	0.0	(−0.00095146, 0.094500, 0)	10.00	317.44	103
Q04	1.45	0.578486	0.394310	0.0	0.0	(−0.00092318, 0.092922, 0)	10.00	317.44	103
Q05	1.50	0.586758	0.386214	0.0	0.0	(−0.00091215, 0.092328, 0)	10.00	317.44	103
Q06	1.60	0.602367	0.370978	0.0	0.0	(−0.00088915, 0.091074, 0)	10.00	317.44	103
Q07	1.75	0.623691	0.350248	0.0	0.0	(−0.00085215, 0.089076, 0)	10.00	317.44	103
Q08	1.90	0.642849	0.331709	0.0	0.0	(−0.00081702, 0.086999, 0)	10.00	317.44	103
Q09	2.00	0.654574	0.320400	0.0	0.0	(−0.00079295, 0.085598, 0)	10.00	317.44	103
Q10	2.05	0.660153	0.315030	0.0	0.0	(−0.00078063, 0.084896, 0)	10.00	317.44	103
Q11	2.20	0.675859	0.299945	0.0	0.0	(−0.00074412, 0.082799, 0)	10.00	317.44	103
Q12	2.35	0.690180	0.286237	0.0	0.0	(−0.00070983, 0.080733, 0)	10.00	317.44	103
Q13	2.50	0.703291	0.273726	0.0	0.0	(−0.00067707, 0.078713, 0)	10.00	317.44	103
H01	1.00	0.487207	0.487207	0.0	0.0	(−0.00071204, 0.090099, 0)	11.00	409.60	200
H02	2.00	0.655683	0.321576	0.0	0.0	(−0.00057168, 0.080204, 0)	11.00	409.60	200
H03	3.00	0.740897	0.239917	0.0	0.0	(−0.00041607, 0.067799, 0)	11.00	409.60	200
H04	4.00	0.792317	0.191313	0.0	0.0	(−0.00030795, 0.057941, 0)	11.00	409.60	200
H05	5.00	0.826040	0.158317	0.0	0.0	(−0.00033261, 0.053831, 0)	10.00	409.60	240
H06	6.00	0.850747	0.135461	0.0	0.0	(−0.00026264, 0.047519, 0)	10.00	409.60	200
H07	7.00	0.869309	0.118371	0.0	0.0	(−0.00021252, 0.042488, 0)	10.00	409.60	320
H08	10.00	0.907397	0.085237	0.0	0.0	(−0.00016852, 0.036699, 0)	8.39	409.60	400
H09	15.00	0.936224	0.057566	0.0	0.0	(−0.00016052, 0.029072, 0)	7.25	409.60	800
S01	1.00	0.453711	0.453711	−0.4	−0.4	(−0.00079326, 0.092237, 0)	11.00	409.60	200
S02	1.00	0.453865	0.453865	0.4	0.4	(−0.00065074, 0.088023, 0)	11.00	409.60	200
S03	1.00	0.303458	0.303458	0.8	0.8	(−0.00060332, 0.086010, 0)	11.00	409.60	200
P01	4.00	0.655334	0.156900	(0.6, 0.0, 0.0)	(−0.6, 0.0, 0.0)	(0, 0.066502, 0)	9.00	409.60	140
P02	4.00	0.655306	0.156762	(0.3, 0.0, −0.5)	(−0.6, 0.0, 0.0)	(0, 0.068787, 0)	9.00	409.60	140
P03	4.00	0.655306	0.156764	(−0.3, 0.0, −0.5)	(−0.6, 0.0, 0.0)	(0, 0.068758, 0)	9.00	409.60	140

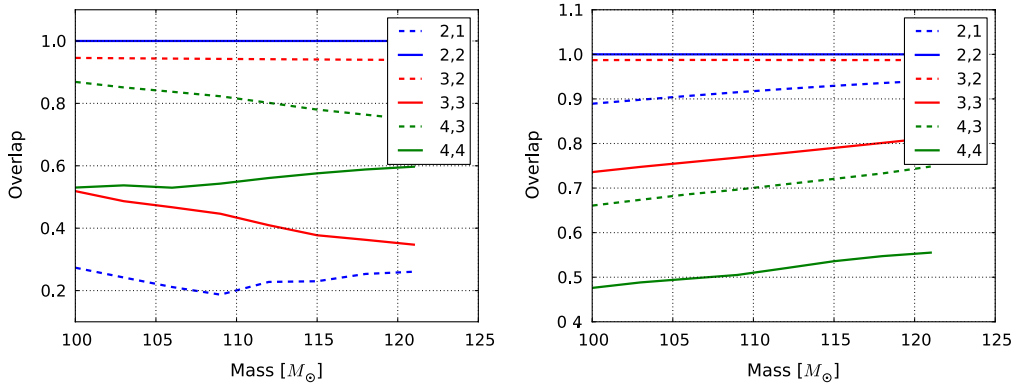

FIG. 4 (color online). Overlap of higher modes with 2,2 for $q = 1$ (left) and $q = 4$ (right) systems. In both cases the most significant higher modes have poor overlaps with (2,2), suggesting that h_{22} will be a poor fit to the full signal in regions dominated by these modes.

$$\rho(s, h, t_0) = \frac{4}{\sqrt{(h_+|h_+)}} \left| \int_0^\infty \frac{\tilde{s}(f)\tilde{h}_+^\star(f)}{S_n(f)} e^{-2\pi i f t_0} df \right|, \quad (6)$$

where the absolute value removes the dependence on the unknown phase. Equation (6) may be evaluated by a single complex inverse Fourier transform, and the maximization over t_0 is then accomplished by finding the maximum of the resulting time series. Equation (6) is only an exact calculation of the SNR if $(h_+|h_\times) = 0$ [15], which is not true in general; however, we expect the errors introduced by this approximation to be small.

Note that, by Eq. (3), the dependence on the SNR of the detector angles may be factored out in Eq. (6). Note also that $F_0(0, 0) = 1$. These imply that, given the SNR of a signal at $\theta = \varphi = 0$, we know the SNR of a signal in the same orientation at all other sky positions.

Related to the SNR is the *match* or *overlap* obtained by normalizing both waveforms:

$$\langle s|h_+\rangle = \max_{t_0,\phi_0} \frac{(s|h_+)}{\sqrt{(s|s)(h_+|h_+)}}. \quad (7)$$

The overlap is a measure from 0 to 1 of how well the template matches the signal; an overlap of 1 indicates that the template is an exact match to the signal and anything lower than 1 is a diminished match.

Gravitational-wave strain falls off as the the reciprocal of the distance between source and detector. It follows from Eq. (5) that the SNR falls off in the same way, while the normalization removes the distance dependence of the template. Henceforth we place the signal s in Eq. (5) at 1 Mpc from the detector and denote the resulting SNR as $\rho_{1\ \mathrm{Mpc}}$. We also choose a *threshold SNR*, a value above which indicates the presence of a signal in the data. We will take this to be 5.5, the threshold used in current LIGO/Virgo searches. The choice of this value is motivated by the behavior of the noise in the detector [16]. The distance at which a signal would have an SNR of 5.5 is then

$$r = \frac{\rho_{1\ \mathrm{Mpc}}}{5.5}. \quad (8)$$

We now consider two templates: h_{ideal} which exactly matches the signal and h which in some way approximates the signal. We can determine the fraction of the available distance that is lost by using the approximate template as

$$\frac{r}{r_{\mathrm{ideal}}} = \frac{\rho_{1\ \mathrm{Mpc}}(h)/5.5}{\rho_{1\ \mathrm{Mpc}}(h_{\mathrm{ideal}})/5.5} = \frac{\langle s|h\rangle}{\langle s|h_{\mathrm{ideal}}\rangle} = \langle s|h\rangle. \quad (9)$$

The first equality follows from Eq. (8), the second from dividing both numerator and denominator by the common factor $(s|s)^{1/2}$ and the third from the fact that when the template exactly matches the signal the overlap is 1. The overlap therefore measures the fraction of the SNR lost by using an incorrect template, and equivalently the fraction of the distance lost. As the Universe is approximately uniform at distances accessible to even initial LIGO [2],

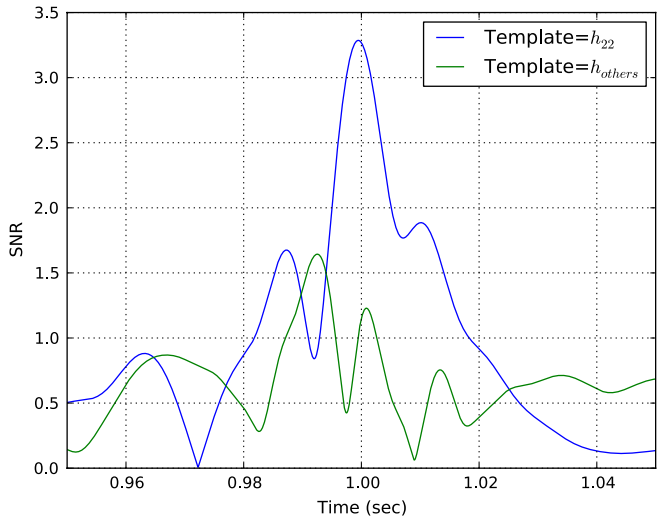

FIG. 5 (color online). SNR time series for $\rho(s, h_{2,2})$ and $\rho(s, h_{\mathrm{others}})$. The specific behavior will depend on the angles; the values here were chosen to illustrate the issue, $\theta = 2.36$, $\varphi = 2.58$, $\iota = 1.54$, $\phi = 5.16$. At the time when the $h_{2,2}$ series peaks, h_{others} has dropped by 38%. The tension between the modes means that the total SNR will be less than the sum of the component SNRs.

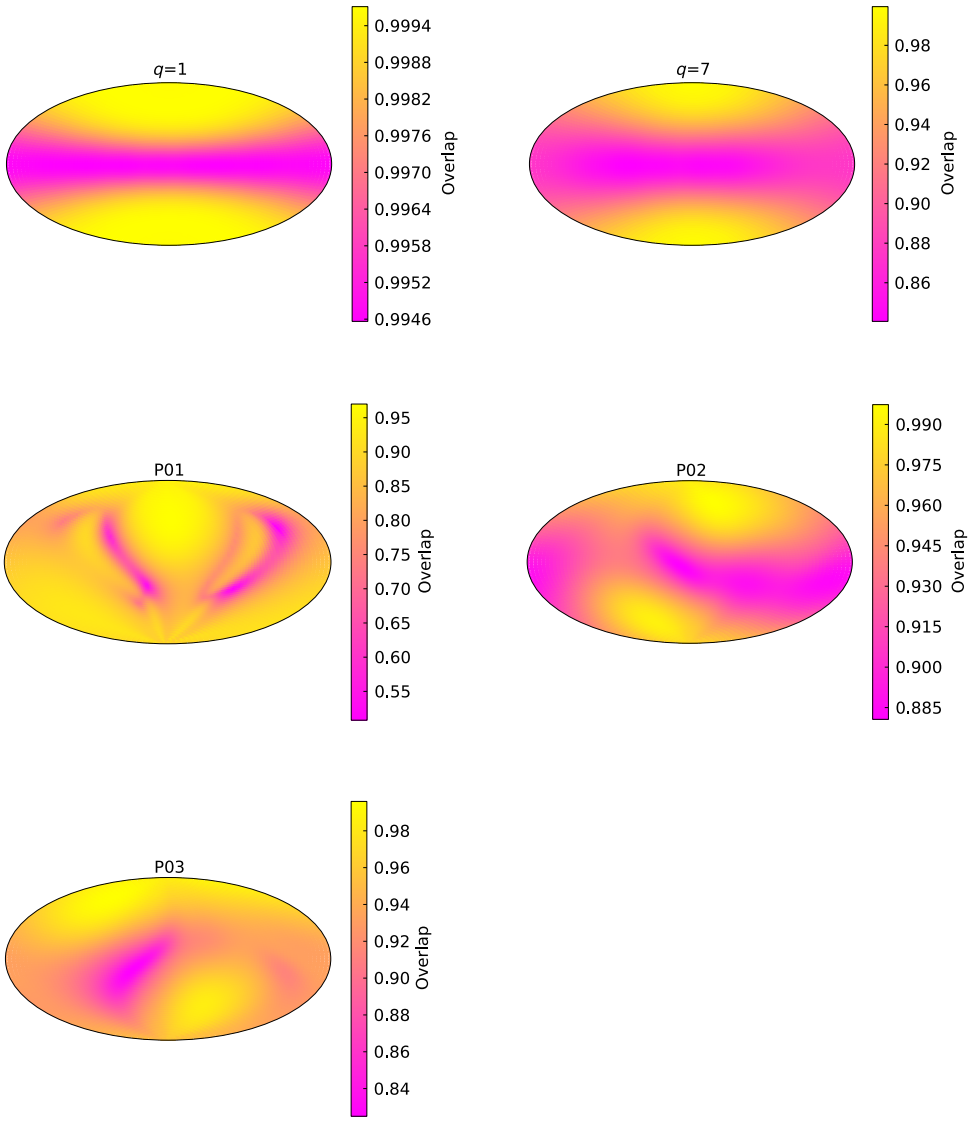

FIG. 6 (color online). Overlaps in source-centric coordinates, ϕ horizontally and ι vertically, between the complete waveform and the (2,2) mode for (top) the nonspinning $q = 1$ and $q = 4$, (middle) the precessing P01 and P02 and (bottom) the precessing P03 signals from Table I. The general features of the nonspinning images are representative of all mass ratios and (anti)aligned spin systems; overlaps are 1.0 at $\iota = 0$, π where the full signal reduces to the (2,2) mode, and are lowest at $\iota = \pi/2$. There is more interesting structure in the precessing cases.

the event rate is approximately equal to the cube of the range, although this will also depend on the antenna pattern. However, we note that the overlap does not give the value of $r_{\rm ideal}$. As an extreme example, if $r_{\rm ideal}$ is sufficiently small that the number of expected events per observation time is close to zero, then the fractional loss of range implied by a low overlap is inconsequential.

III. THE BINARY BLACK HOLE COALESCENCE WAVEFORMS

This paper uses NR waveforms covering the late inspiral, merger and ringdown for a variety of mass ratios and spins. All of the NR simulations used in this study were produced with GATech's MAYA code [17–22]. The MAYA code uses the Einstein Toolkit [23] which is based on the CACTUS [24] infrastructure and CARPET [25] mesh refinement. Evolution thorns were generated with the KRANC [26] code generator. We use sixth-order spatial finite differencing and extract the waveforms at a finite radius of $75M$, where M is a code unit set to unity and can be scaled to any physical mass scale. All grids have ten levels of refinements unless noted below.

We use 28 simulations in this paper and group them according to their initial parameters in Table I. Grid details, including outer boundary and resolution on the finest grid are also shown. The simulations can be separated into three groups: nonspinning, equal mass with aligned spin, or

unequal mass with precessing spin. For the simulations with $q > 4$, we used the coordinate-dependent gauge term as described in Refs. [27,28]. For the $q = 10$ and $q = 15$ simulations, initial parameters in Ref. [29] were used. These simulations ($q > 4$) have an extra level of refinement for 11 levels total, with the exception of $q = 6$ and $q = 15$. These have 10 levels and 12 levels, respectively. Another approach to generating complete numeric waveforms with particular attention to the (2,2), (3,3), and (2,1) modes has been studied in Ref. [30].

The output of all simulations is the Weyl scalar, Ψ_4, decomposed into spin-weighted spherical harmonics. Simulations are performed in a coordinate system which we will denote the *source-centric* frame, to distinguish it from the *detector-centric* frame we will employ subsequently. See Fig. 2 for the definition of the angles used in this frame. In terms of these angles the decomposition is

$$rM\Psi_4(\iota, \phi, t) = \sum_{l,m} {}_{-2}Y_{\ell m}(\iota, \phi) C_{\ell m}(t). \quad (10)$$

This is related to the strain measured by gravitational-wave observatories as

$$\begin{aligned}\Psi_4(\iota, \phi, t) &= -(\ddot{h}_+(\iota, \phi, t) - i\ddot{h}_\times(\iota, \phi, t)) \\ &= \sum_{\ell m} {}_{-2}Y_{\ell m}(\iota, \phi)\ddot{h}^\star_{\ell m}(t). \end{aligned} \quad (11)$$

The quadrupole mode is given by $(\ell, |m|) = (2, 2)$. Throughout this paper we work in the frequency domain, and therefore avoid the integration to strain since $\tilde{h} = \tilde{\Psi}_4/(-4\pi^2 f^2)$.

IV. OVERLAP

We start by examining the relative importance of the non-dominant modes in a waveform comparison. The full waveform involves factors of the spherical harmonics and the amplitudes of the modes [see Eq. (10)]. When the amplitudes of the higher modes are vanishingly small, they can be ignored; however, as we have already noted in Fig. 1, the relative amplitudes grow in strength with mass ratio.

In Fig. 4 we plot the overlap of each mode against (2,2) individually. If all modes matched well against (2,2) it would suggest that a template containing only this mode would be a good match to the full signal, regardless of the source orientation; however, we find that not to be the case. In both the $q = 1$ and $q = 4$ cases, the overlap between (2,2) and the next most dominant modes is poor, below 0.6. Furthermore, although the inner product, Eq. (4), and the decomposition into modes, Eq. (10), are themselves linear, the maximization over time and phase introduces nonlinearities. In particular, defining $h_{\rm others} = \sum_{l,m\neq 2,2} h_{lm}$, the sum is only linear if the inner products maximize at the same time. If not, there will be a "tension" in the modes and the combined SNR will be less than the sum of the individual SNRs, i.e.,

$$\rho^2(s, h) \neq \rho^2(s, h_{22}) + \rho^2(s, h_{\rm others}). \quad (12)$$

TABLE II. Summary values of the overlaps between the (2,2) mode and the full template as a function of the orientation angles (ι, ϕ). Names in parenthesis refer to Table I. Note that the P01 precessing system has lower overlaps, and a smaller fraction of overlaps greater than 0.97, than the other systems.

ID	q	χ	% of area ≥ 0.97	Average	Median	Minimum
H01	1	0	100	0.997	0.998	0.995
H03	3	0	27	0.955	0.951	0.918
H04	4	0	18	0.937	0.931	0.885
H05	5	0	16	0.927	0.920	0.868
H06	6	0	13	0.916	0.907	0.847
H07	7	0	11	0.907	0.898	0.840
H08	10	0	11	0.903	0.892	0.826
H09	15	0	11	0.897	0.886	0.817
S01	1	−0.4	100	0.997	0.997	0.993
S02	1	0.4	100	0.997	0.997	0.994
S03	1	0.8	100	0.997	0.997	0.994
P01	4	0.6 (90°)	0.01	0.844	0.861	0.498
P02	4	0.6 (150°)	17	0.937	0.937	0.880
P03	4	0.6 (210°)	14	0.933	0.934	0.824

To quantify this we plot the time series of both SNRs on the right-hand side of Eq. (12) in Fig. 5. The two series peak at notably different times, and at the peak of the h_{22} series the $h_{\rm other}$ series has dropped by 38%; thus we can conclude that the nonlinearities are important, and we cannot use the linear approximation.

While Fig. 4 shows that the (2,2) mode is not an effective representation of the other modes, how well does the (2,2) mode cover the sky of the source? The overlap between the full-mode waveform and the (2,2) mode is a function of

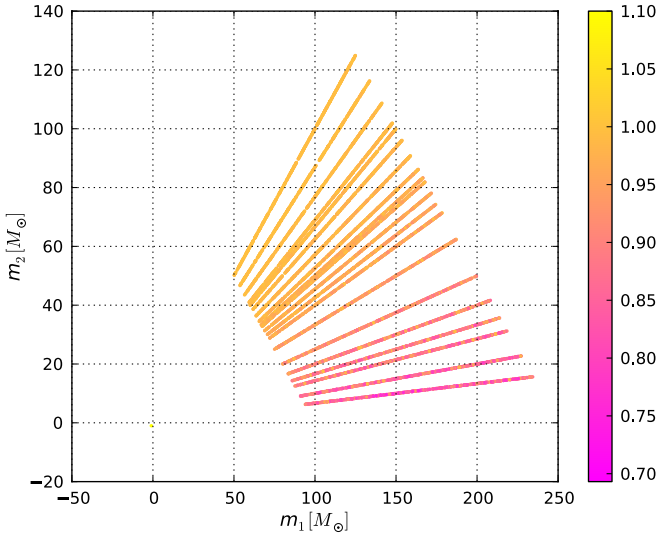

FIG. 7 (color online). Overlaps between the complete waveform and the (2,2) mode for nonspinning waveforms with mass ratios from 1 to 15, with all angles and total mass chosen randomly. At higher mass ratios more of the total power is distributed into the higher modes and the match drops accordingly.

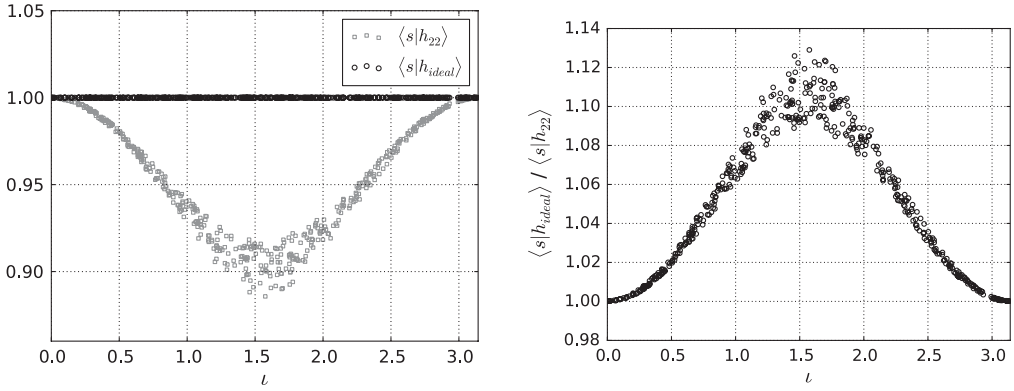

FIG. 8. Left: The overlaps obtained using both templates. Since $h_{\rm ideal} = s$ the overlap is 1. Right: The ratio of the overlaps. This is identical to the ratio of SNRs as the additional factors of $(s|s)$ cancel.

the angles centered at the source, (ι, ϕ). The (2,2)-only template depends on the angles through a single factor, ${}_2Y_{22}(\iota, \phi)$, which is canceled by the normalization; therefore, we simplify the overlap by placing this waveform at $\iota = \phi = 0$. We also place both waveforms optimally in the sky of the detector, at $\theta = \varphi = 0$, and choose $\psi = 0$. We will generalize this momentarily. Figure 6 shows the resulting overlaps for five cases: the nonspinning $q = 1$ and $q = 7$, and the precessing cases from Table I. At $\iota = 0, \pi$ the waveform is dominated by the (2,2) modes; the overlap approaches 1.0 at these points. Equation (9) then implies that there is no loss of distance incurred by searching with the (2,2)-only template for systems that are oriented face-on with respect to the detector. We can further quantify this by determining the fraction of surface area over which the overlap falls below 0.97%, where this value is motivated by the allowed 3% loss of SNR from using a discrete set of templates [2]. Table II lists this value for several simulations, along with the the average, median and lowest overlaps as further measures of the impact of the higher modes.

Figures 5–7 and Table II all tell the same story for a single detector when the intrinsic parameters are kept fixed to the signal: the $q = 1$ case is well served with a (2,2)-only waveform over all source angles. The higher the mass ratio, the worse a (2,2)-only waveform does in matching the signal, and this fraction of angles over which the match does poorly increases. Furthermore, a precessing system is badly served by a (2,2) waveform. We will explore this matter further in future work.

We now generalize the previous results to include other values of the detector-centric angles (θ, φ) and ψ. Consider two templates: h_{22} which, as in current searches, contains only the (2,2) mode of the NR waveform optimally oriented ($\theta = \varphi = \iota = \phi = \psi = 0$), and a perfect template $h_{\rm ideal}$ which exactly matches the signal. In Fig. 7 we show the overlap between the signal and h_{22} for several nonspinning systems. Each colored line on the graph represents a system mass ratio; moving along the line gives different system masses. As we move from top to bottom, we are moving from $q = 1$ to $q = 15$. The difference in colors along the line gives the overlap value. The plot shows that for higher mass ratios the total power is distributed into the higher modes and the match drops accordingly. This is consistent with Refs. [8,12].

Now consider the $q = 4$ nonspinning system, scaled to $100M_\odot$ and placed at a distance of 1 Gpc from the detector, and examine the overlap between the signal and both templates. We randomly choose values for all angles and plot results with respect to ι, which has the most significant dependence. The results are shown in Fig. 8, which illustrates that at $\iota = 0, \pi$ the variation of the additional angles does not affect the overlap, while the spread in results widens towards $\iota = \pi/2$. This again shows that the (2,2) mode only captures a face-on source orientation and misses the source as its inclination increases toward the edge-on case. This would imply that the higher modes are essential for detecting nonoptimally oriented signals, but how far away can a single detector see these cases? We quantify how important the modes will be in terms of SNR and volume reach in the next section.

V. SNR AND VOLUME

As noted at the end of Sec. II, the overlap is equal to the fractional loss in distance to which a signal can be detected, but this value should be viewed in light of the maximum possible distance. This maximum distance depends on three factors: (1) the total energy radiated by the source, (2) the ability of the template to extract energy of the signal from the background noise and (3) the location of the source in the sky of the detector. For example, in the plane of the detector along the lines 45° to the arms, the response goes to zero. Along these lines the loss in range implied by a low overlap is irrelevant for a single detector. In this section we consider the accessible distances, noting the influence of all three factors.

We start with Fig. 9, which shows the radiated energy and distances accessible using the $h_{\rm ideal}$ templates, as a function of the source orientation. As expected, the range tends to be lowest where the least power is radiated,

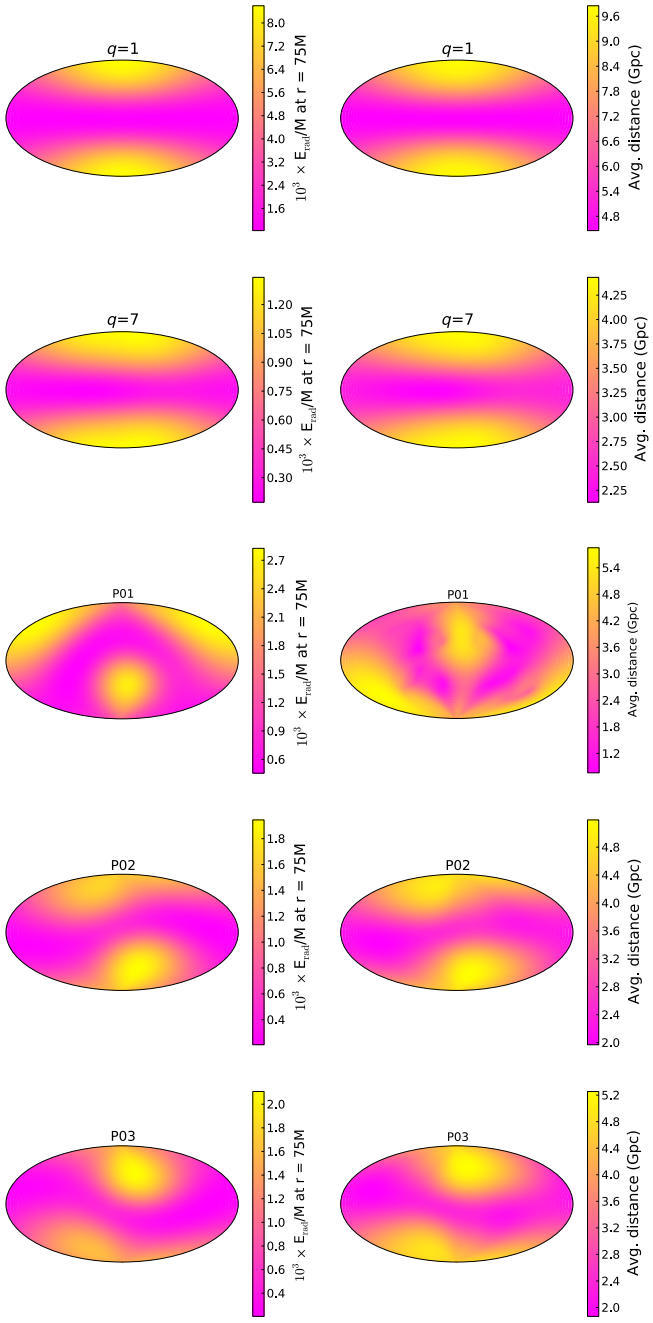

FIG. 9 (color online). Radiated energy and distances to which signals are visible using the optimal template, in source-centric coordinates ϕ horizontally and ι vertically. Top to bottom: $q = 1$, $q = 7$, and the precessing P01, P02 and P03 systems. Note that the structure is similar to the overlaps between the full signal and the h_{22} template [Fig. 6].

although the energy and distance plots are not identical due to weighting by the noise curve. The energy (and hence distance) plots have the same general shape as those corresponding in Fig. 6, indicating that the overlaps between the signal and h_{22} are lowest at orientations where the energy and distance reach of the ideal template are also lowest. This is due to the fact that the higher modes

TABLE III. Sensitivity volumes and average distances achievable using both templates. ID values correspond to Table I. Angles following spin magnitude indicate the initial angle of the spin vector of the larger hole in the x, z plane; such systems exhibit precession. Spins not followed by an angle indicate the spins are (anti)aligned with the orbital angular momentum and the system does not precess. Volumes are reduced with increased q and anti-aligned spins, and increased with align spins due to the total power radiated in-band. For higher q the use of the ideal template expands the volume by up to 30% for the systems considered here, although the fractional improvement is greatest for the systems where the volume accessible with $h_{\rm ideal}$ is smallest.

ID	q	a	Volume using h_{22} (Gpc^3)	$R_{\rm avg}$ using h_{22} (Gpc)	Volume using $h_{\rm ideal}$ (Gpc^3)	$R_{\rm avg}$ using $h_{\rm ideal}$ (Gpc)
H01	1	0.0	217	3.3	218	3.4
H03	3	0.0	91	2.5	102	2.6
H04	4	0.0	57	2.2	68	2.3
H05	5	0.0	39	1.9	47	2.0
H06	6	0.0	27	1.7	34	1.8
H07	7	0.0	19	1.5	25	1.6
H08	10	0.0	9.3	1.2	12	1.3
H09	15	0.0	3.3	0.8	4.3	0.9
S01	1	−0.4	165	3.1	166	3.1
S02	1	0.4	313	3.8	315	3.8
S03	1	0.8	458	4.3	461	4.3
P01	4	0.6 (90°)	55	2.1	80	2.4
P02	4	0.6 (150°)	34	1.8	41	1.9
P03	4	0.6 (210°)	34	1.8	41	1.9

not only have poor matches with (2,2), as shown in Fig. 4, but they also contain less power, as shown in Fig. 1. Figure 9 shows that orientations where the higher modes dominate have both low matches with h_{22} and lower

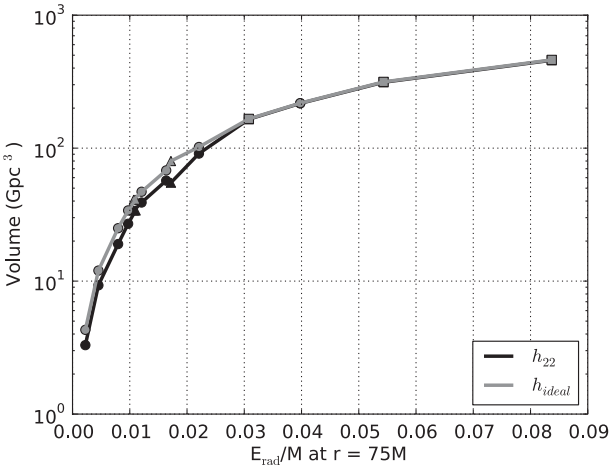

FIG. 10. Correlation between the total energy radiated from $r = 75M$ by the systems in Table III and the accessible volumes using the h_{22} and $h_{\rm ideal}$ templates. Circles are nonspinning systems, squares are spinning but nonprecessing systems, and triangles are precessing systems. The P02 and P03 systems have close to identical values of $E_{\rm rad}$ and volumes; these points therefore lie on top of each other. The h_{22} template gives a notably smaller fraction of the volume for the P01 system than for any other; this corresponds directly to the lower overlap noted in Table II.

ranges. This indicates that the fractional loss in distance incurred by using the incorrect template is greatest where the best possible range is smallest.

Finally, in order to characterize the performance of different templates by a single number with physical significance we calculate the spatial volume to which the search is sensitive. The distance to which a signal can be seen depends on all five angles, but from Eq. (3) and the comments at the end of Sec. II the dependence on the detector-centric angles may be factored out:

$$R(\theta, \varphi, \iota, \phi, \psi) = F_0(\theta, \varphi)R(\iota, \phi, \psi). \tag{13}$$

Since there is no preferred orientation we define an *average visibility range*, R, by averaging the distances over the orientation angles ι, ϕ, ψ:

$$R = \frac{1}{N}\sum_i^N \frac{\rho(s(\iota_i, \phi_i, \psi_i), h)}{5.5}. \tag{14}$$

We evaluate this average by choosing random values for ι, $\cos(\phi)$, ψ uniform in $(0, 2\pi)$, $(-1, 1)$, $(0, 2\pi)$ respectively.

The average visibility distance as a function of the detector-centric angles is therefore

$$R(\theta, \varphi) = RF_0(\theta, \varphi) \tag{15}$$

and the volume of the Universe to which a given template is sensitive is therefore

$$\begin{aligned} V &= \int_0^{2\pi} d\varphi \int_0^{\pi} \sin(\theta) d\theta \int_0^{R(\theta,\varphi)} r^2 dr \\ &= \frac{1}{3}\int_0^{2\pi} d\varphi \int_0^{\pi} \sin(\theta) d\theta R^3(\theta, \varphi) \\ &= \frac{R^3}{3}\int_0^{2\pi} d\varphi \int_0^{\pi} \sin(\theta) d\theta F_0^3(\theta, \varphi). \end{aligned} \tag{16}$$

The remaining integral may be done numerically, yielding a value ≈ 3.687.

The volumes for different waveforms, using the h_{22} and $h_{\rm ideal}$ templates, are summarized in Table III. The trend is for lower mass ratios and higher aligned spins to correspond to both larger absolute volumes and smaller relative differences by including higher modes in the template. The larger volumes correspond directly to the increased total energy radiated by such systems, which is shown in Fig. 10.

Finally, as another way of quantifying the difference between the templates, in Fig. 11 we show histograms of the visibility ranges over the complete set of orientations at $\theta = \varphi = 0$. Using $h_{\rm ideal}$ shifts the ranges from lower to higher values somewhat, but does not increase the maximum distance, which occurs for face-on systems which are dominated by (2,2).

These results include three precessing $q = 4$, $a = 0.6$ systems. In all cases the accessible volume is less than that for the $q = 4$ nonspinning system. As might be expected from the nonprecessing cases the volume decreases as the

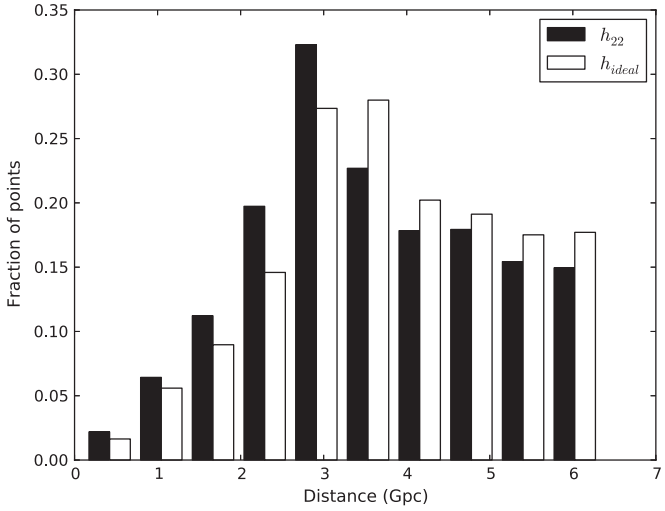

FIG. 11. Histograms showing the distributions of distances using both templates for the $q = 4$ system. Using $h_{\rm ideal}$ shifts points from lower distances to higher, but does not increase the maximum range.

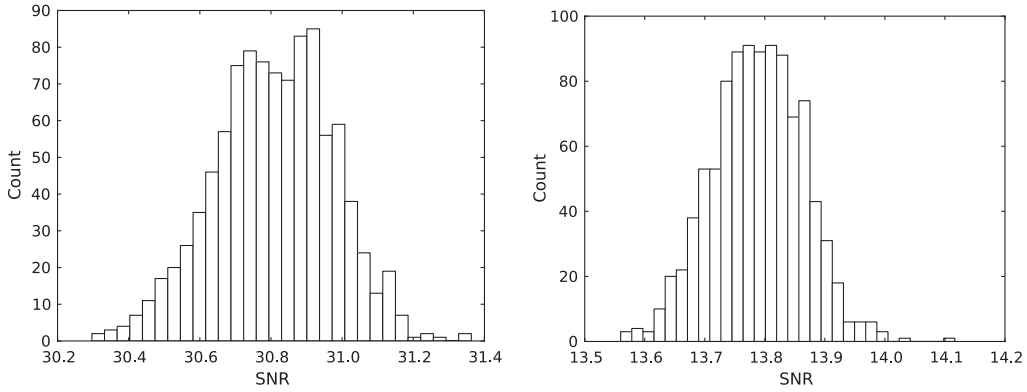

FIG. 12. Histograms showing variation in distance along the $\theta = \varphi = 0$ sky direction for (left) $q = 1$ and (right) $q = 7$ systems. For $q = 1$ the mean is 30.80, corresponding to a distance of 5.6 Gpc, and the standard deviation is 0.17. For $q = 7$ the mean is 13.79, corresponding to 2.51 Gpc, and the standard deviation is 0.08.

TABLE IV. Volumes obtained using the $q = 4$ system and $h_{\rm ideal}$ template for various extraction radii and simulation resolutions. All values are in Gpc^3. All of these runs used the same set of points. There is a general trend downward with decreased resolution and increased extraction radius. The latter effect is due to the fact that the late inspiral, merger and ringdown portions of the waveform get smaller as $r \to \infty$. Although the inspiral portion actually increases as $r \to \infty$, since the majority of the power radiated is in the last orbits and merger the volume decreases. As the variation is small we expect the difference from the true value to be small as well.

	Resolution		
Extraction radius	M/160	M/180	M/200
60 M	69.59	69.62	69.64
75 M	69.12	69.14	69.16
100 M	68.57	68.59	68.61

spin becomes anti-aligned with the angular momentum and less total energy is radiated. However, at least for the systems considered here, this dependence becomes smaller than our uncertainties when the angle between the orbital angular momentum and the spin of the larger hold exceeds 150°.

A. Error analysis

Because we choose random values in evaluating the average Eq. (14) we are able to determine the error in the results as the standard deviation between several runs. Because of the computational expense of complete runs we instead estimate this by choosing one sky position. We show the SNR histograms obtained by 900 runs of $\theta = \varphi = \pi/3$ for two waveforms in Fig. 12. In both cases the error is on the order of 0.5%. Since $V = r^3$ and r has an error δr, then $\delta V = \sqrt{((dV/dr)\delta r)^2}$. Here we have $\delta V/V = 3\delta r/r$. The error for the results in Table III is then on the order of 1.5%. There are also uncertainties associated with the choice of extraction radius and resolution. We show the volumes obtained using the $q = 4$ systems and $h_{\rm ideal}$ template for several values of both parameters in Table IV. The variation is on the order of 1.5%, and our two sources of uncertainty are comparable and small enough that they do not affect our conclusions.

VI. CONCLUSIONS

As can be seen from Table III there are two conflicting trends as the mass ratio increases. As the total radiated energy is reduced, the volume drops. Conversely, as the fraction of this energy is distributed into higher modes the benefit gained by using the ideal template increases. The energy radiated (and hence volume) increases with spin. Together, these results imply a strong bias towards the detection of equal-mass, aligned-spin systems when averaged over the sky. This conclusion is consistent with Refs. [31,32], while adding the fact that the inclusion of higher modes is not important for detecting these systems. We expect that a search using (2,2) IMRPhenB aligned-spin templates will perform well; this will be tested as part of the ongoing NINJA2 project [33].

For nonspinning systems with $q \gtrsim 3$ and the mildly precessing systems considered here, the inclusion of higher modes in the template can improve the volume reach of the single detector. Whether or not this translates to an increase in detection rate depends on the unknown underlying rates of such systems. Put another way, the inclusion of higher modes in templates will allow the advanced detector network to better measure or bound these unknown rates.

There are, however, some caveats. First, we stress that the template used for the rightmost column of Table III exactly matches the signal; that is, it assumes we exactly know the signal for which we are looking in advance. To the extent that matched filtering is the optimal detection statistic any approximate inclusion of higher mode information will of necessity do worse. Furthermore, there are potential downsides to including higher modes in the templates. Such an addition would require increasing the number of templates. This entails a corresponding increase in the computational cost of the search. In addition, these additional templates may respond to glitches in the detector, raising the number of "background" events and increasing the SNR at which a signal would need to be observed in order to confidently claim a detection. Concerns such as this lead to changing the mass range in the S6 search from $35M_\odot$ to $25M_\odot$—the templates at the higher-mass end produced sufficient numbers of background triggers to impair the ability to detect lower-mass systems [1]. It would be undesirable to allow a search for systems to which the detector network is comparatively insensitive to impact the ability to detect equal-mass and aligned-spin systems. We also note that, at present, it is not known how to construct a template bank of precessing signals. Further studies are needed to determine the right strategy for detecting both mildly and heavily precessing systems.

We have not yet considered spinning systems with $q > 1$. Such simulations are available for spins up to 0.6 and mass ratios up to 7; however, we defer their analysis to future work. For spins aligned with the angular momentum the volumes accessible will certainly be larger than the nonspinning counterparts. It is possible that the dependence on higher modes will be preserved in these cases, leading to a potentially large volume increase by using templates that include higher modes.

We have so far considered only a single detector. Additional detectors will provide better sky coverage, effectively increasing the value of the integral in Eq. (16). Furthermore, as noted in the introduction, detectors oriented differently are sensitive to different polarizations; it is therefore conceivable that the inclusion of

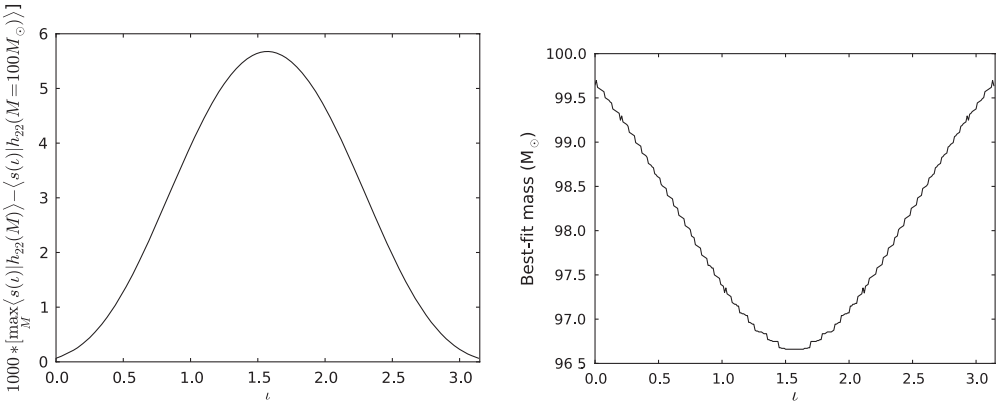

FIG. 13. Effect of higher modes on parameter recovery. Left: The difference in overlap obtained by maximizing over the mass of the template. Right: The value of the mass which maximizes the overlap. The largest differences are at $\iota = \pi/2$, where the system is edge-on and the $(2, \pm 2)$ modes are most suppressed.

higher modes in templates would have more impact on the range of the network as a whole than on any one detector. We have also not considered other aspects of the full search, such as signal-based vetoes. The effect of such vetoes is being studied in Ref. [34].

One important aspect of gravitational-wave detection we have also not considered is the fact that the data are filtered against a bank of templates with different parameters. For the initial detection it is acceptable for the signal to be picked up by a template with the wrong parameters; once the detection has been confirmed more computationally expensive parameter estimation codes can be run. While this freedom cannot raise the volume accessible to $h_{\rm ideal}$, as it is already a perfect match to the signal, it is quite possible that maximization over a bank of h_{22} templates will lead to larger average SNRs and hence volumes. In this case the fractional gain by going to an approximation of $h_{\rm ideal}$ may be even smaller.

This last point leads to the question of the importance of higher modes in parameter estimation. We expect higher modes to be important here; as a simple example the difference between a signal at $\iota = \psi = \pi/4$ and one at $\iota = \psi = 0$ is entirely encapsulated in the mode content. We expect that there are degeneracies between the orientation parameters and intrinsic parameters; we intend to investigate this further in subsequent studies. However we present a preliminary result in Fig. 13, which shows that $\langle s(\iota, \psi)|h_{22}\rangle$ can be increased by maximizing over the mass M of the template, at the cost of misestimating the mass. The increase in overlap is most pronounced at $\iota = \pi/2$, where the higher modes are most significant. Correspondingly the mass which maximizes the overlap deviates the most from the true value at this point. This suggests a degeneracy between mass and higher-mode content. One possible explanation is that the higher modes contain more power at higher frequencies, as do lower-mass systems. We will explore this possibility in our follow-up studies.

ACKNOWLEDGMENTS

Work supported by NSF Grants No. 0914553, No. 0941417, No. 0903973, and No. 0955825. Computations at Teragrid TG-PHY120016, CRA Cygnus cluster and the Syracuse University Gravitation and Relativity cluster, which is supported by NSF Grants No. PHY-1040231, No. PHY-0600953 and No. PHY-1104371. This research was supported in part by the National Science Foundation under Grant No. NSF PHY11-25915. We also would like to thank Stephen Fairhurst and Duncan Brown for their comments.

[1] LIGO Scientific Collaboration and Virgo Collaboration, arXiv:1203.2674.
[2] LIGO Scientific Collaboration and Virgo Collaboration, Phys. Rev. D **85**, 082002 (2012).
[3] S. Fairhurst, arXiv:1205.6611.
[4] K. Thorne, *300 Years of Gravitation* (Cambridge University Press, Cambridge, England, 1987).
[5] The LIGO Scientific Collaboration, Report No. LIGO-T0900288-v3, LIGO Project 2009, https://dcc.ligo.org/DocDB/0002/T0900288/003/AdvLIGO20curves.pdf.
[6] D. Shoemaker, B. Vaishnav, I. Hinder, and F. Herrmann, Classical Quantum Gravity **25**, 114047 (2008).
[7] B. Vaishnav, I. Hinder, F. Herrmann, and D. Shoemaker, Phys. Rev. D **76**, 084020 (2007).

[8] S. T. McWilliams, B. J. Kelly, and J. G. Baker, Phys. Rev. D **82**, 024014 (2010).
[9] P. Ajith, M. Boyle, D. A. Brown, B. Brugmann, L. T. Buchman *et al.*, Classical Quantum Gravity **29**, 124001 (2012).
[10] P. Ajith, S. Babak, Y. Chen, M. Hewitson, B. Krishnan, A. M. Sintes, J. T. Whelan, B. Brügmann, P. Diener, N. Dorband *et al.*, Phys. Rev. D **77**, 104017 (2008).
[11] Y. Pan, A. Buonanno, L. T. Buchman, T. Chu, L. E. Kidder, H. P. Pfeiffer, and M. A. Scheel, Phys. Rev. D **81**, 084041 (2010).
[12] D. A. Brown, P. Kumar, and A. H. Nitz, arXiv:1211.6184.
[13] W. G. Anderson, P. R. Brady, J. D. E. Creighton, and E. E. Flanagan, Phys. Rev. D **63**, 042003 (2001).
[14] D. A. Brown, A. Lundgren, and R. O'Shaughnessy, Phys. Rev. D **86**, 064020 (2012).
[15] S. Babak, R. Biswas, P. Brady, D. Brown, K. Cannon *et al.*, Phys. Rev. D **87**, 024033 (2013).
[16] B. Allen, W. G. Anderson, P. R. Brady, D. A. Brown, and J. D. Creighton, Phys. Rev. D **85**, 122006 (2012).
[17] R. Haas, R. V. Shcherbakov, T. Bode, and P. Laguna, Astrophys. J. **749**, 117 (2012).
[18] J. Healy, T. Bode, R. Haas, E. Pazos, P. Laguna *et al.*, arXiv:1112.3928.
[19] T. Bode, P. Laguna, and R. Matzner, Phys. Rev. D **84**, 064044 (2011).
[20] T. Bode, T. Bogdanovic, R. Haas, J. Healy, P. Laguna, and D. Shoemaker, Astrophys. J. **744**, 45 (2012).
[21] T. Bode, R. Haas, T. Bogdanovic, P. Laguna, and D. Shoemaker, Astrophys. J. **715**, 1117 (2010).
[22] J. Healy, J. Levin, and D. Shoemaker, Phys. Rev. Lett. **103**, 131101 (2009).
[23] Einstein Toolkit: http://www.einsteintoolkit.org.
[24] Cactus Computational Toolkit: http://www.cactuscode.org.
[25] E. Schnetter, S. H. Hawley, and I. Hawke, Classical Quantum Gravity **21**, 1465 (2004).
[26] S. Husa, I. Hinder, and C. Lechner, Comput. Phys. Commun. **174**, 983 (2006).
[27] D. Muller, J. Grigsby, and B. Bruegmann, Phys. Rev. D **82**, 064004 (2010).
[28] E. Schnetter, Classical Quantum Gravity **27**, 167001 (2010).
[29] H. Nakano, Y. Zlochower, C. O. Lousto, and M. Campanelli, Phys. Rev. D **84**, 124006 (2011).
[30] L. T. Buchman, H. P. Pfeiffer, M. A. Scheel, and B. Szilágyi, Phys. Rev. D **86**, 084033 (2012).
[31] C. Reisswig, S. Husa, L. Rezzolla, E. N. Dorband, D. Pollney, and J. Seiler, Phys. Rev. D **80**, 124026 (2009).
[32] R. O'Shaughnessy, B. Vaishnav, J. Healy, and D. Shoemaker, Phys. Rev. D **82**, 104006 (2010).
[33] M. Frei, C. Hanna, K. Cannon, N. Fotopoulos, D. Keppel, R. Matzner, L. Pekowsky, S. Privitera, A. J. Weinstein, and J. T. Whelan (to be published).
[34] C. Capano, A. Buonanno, and Y. Pan (to be published).